Characterizing frontal eddies along the East Australian Current from HF radar observations

Amandine Schaeffer, A. Gramoullé, M. Roughan, A. Mantovanelli

RESEARCH ARTICLE

Key Points:
- Cyclonic eddies occur frequently along the East Australian Current (30°S) on average every 7 days over a 12 month period
- Frontal eddies with high Rossby number (0.6–1.9) and inshore radius ∼10 km propagate downstream all year round at 0.3–0.4 m/s
- Cyclonic frontal eddies influence biology through vertical uplift favoring local production or entrainment of productive water over 100s of km

Supporting Information:
- Supporting Information S1

Correspondence to:
A. Schaeffer,
a.schaeffer@unsw.edu.au

Characterizing frontal eddies along the East Australian Current from HF radar observations

Amandine Schaeffer[1] , A. Gramoulle[1], M. Roughan[1,2] , and A. Mantovanelli[1]

[1]Coastal and Regional Oceanography Laboratory, School of Mathematics and Statistics, UNSW, Sydney, New South Wales, Australia, [2]Sydney Institute of Marine Science, Mosman, New South Wales, Australia

Abstract The East Australian Current (EAC) dominates the ocean circulation along south-eastern Australia, however, little is known about the submesoscale frontal instabilities associated with this western boundary current. One year of surface current measurements from HF radars, in conjunction with mooring and satellite observations, highlight the occurrence and propagation of meanders and frontal eddies along the inshore edge of the EAC. Eddies were systematically identified using the geometry of the high spatial resolution (∼1.5 km) surface currents, and tracked every hour. Cyclonic eddies were observed irregularly, on average every 7 days, with inshore radius ∼10 km. Among various forms of structures, frontal eddies associated with EAC meanders were characterized by poleward advection speeds of ∼0.3–0.4 m/s, migrating as far as 500 km south, based on satellite imagery. Flow field kinematics show that cyclonic eddies have high Rossby numbers (0.6–1.9) and enhance particle dispersion. Patches of intensified surface divergence at the leading edge of the structures are expected to generate vertical uplift. This is confirmed by subsurface measurements showing temperature uplift of up to 55 m over 24 h and rough estimates of vertical velocities of 10s of meters per day. While frontal eddies propagate through the radar domain independently of local wind stress, upfront wind can influence their stalling and growth, and can also generate large cold core eddies through intense shear. Such coherent structures are a major mechanism for the transport and entrainment of nutrient rich coastal or deep waters, influencing physical and biological dynamics, and connectivity over large distances.

1. Introduction

Far from being steady and laminar, ocean currents are usually characterized by instabilities, meandering, and eddy shedding at different spatial and temporal scales. For instance, variability of the Florida Current transport ranges from high-frequency energy (O(days)) to annual and climate scales [*Meinen et al.*, 2010]. The East Australian Current (EAC) is a southern hemisphere western boundary current (WBC), closing the subtropical gyre in the South Pacific. Its temporal variability is associated with eddy-scale, seasonal, interannual, decadal, and climate scales [*Ridgway*, 2007; *Ridgway et al.*, 2008; *Cetina-Heredia et al.*, 2014; *Sloyan et al.*, 2016], however little is known about time scales on the order of days. Similarly, while mesoscale warm core (anticyclonic) and cold core (cyclonic) eddies have been widely studied, knowledge of submesoscale meanders and frontal eddies is sparse, despite their signature in sea surface temperature and ocean color imagery (e.g., Figure 1).

The EAC forms around 10–20°S in the Coral Sea, accelerates and flows poleward along eastern Australia until it separates from the coast into an eastward flow around 30–32°S [*Cetina-Heredia et al.*, 2014; *Schaeffer and Roughan*, 2015] and a field of southward propagating eddies (Figure 1) [*Everett et al.*, 2012]. Latest observations estimate the mean poleward transport to be around 22 Sv at 27°S above 2000 m, with dominant temporal variability around 60 and 120 days [*Sloyan et al.*, 2016]. Large (O(100–300 km)) warm core eddies [*Nilsson and Cresswell*, 1980] are shed in the region at intervals of 3–6 months [*Wilkin and Zhang*, 2007] and propagate southward over years and distances of O(1000 km) [*Baird and Ridgway*, 2012]. Cyclonic eddies are usually smaller and live for shorter times from days to months [*Oliver et al.*, 2015].

Large 100 km diameter cold core eddies (CCEs) were investigated in modeling studies by *Oke and Griffin* [2011] and *Macdonald et al.* [2016]. Their structures originated from an EAC frontal eddy (referred to as a billow in *Macdonald et al.* [2016]) before growing. The primary source of energy for the growth of the cyclonic
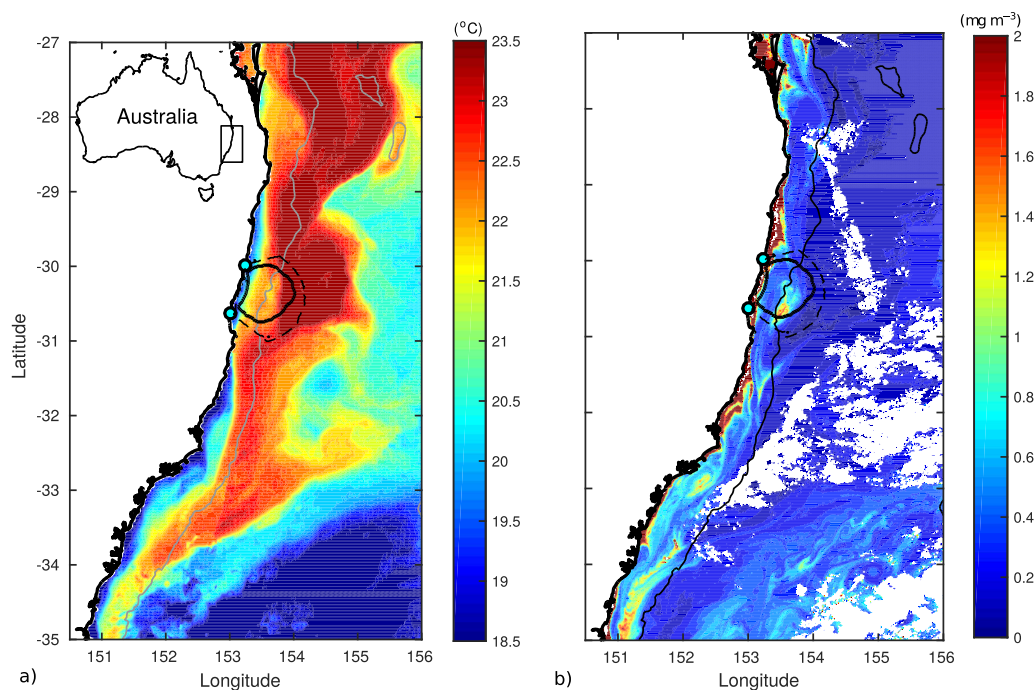
Figure 1. (a) Sea surface temperature (AVHRR L3S product) and (b) ocean color chlorophyll-a concentration (MODIS) remote sensed images on 27 September 2013 over southeastern Australia. The coastline and 2000 m isobaths are shown. Blue dots indicate the location of the two HF Radar systems, black lines show the contours of the spatial coverage for 80% of temporal coverage in the original data set (dashed), and the final coverage used after quality control (continuous line).

eddy appeared to be barotropic instability of the EAC, rather than baroclinic or wind-driven processes. Propagating frontal eddies are also suggested to be the origin of a 90 km diameter eddy sampled at 33.2°S [*Mullaney and Suthers*, 2013] and a smaller CCE of 30 km diameter that was sampled by *Everett et al.* [2011] around 34°S in the austral spring. The latter structure was >300 m deep and moved south at a rate of 15–35 km d^{-1} with a tangential velocity of 0.5 ms^{-1} and a Rossby number of 0.5. The authors suggest that it was likely formed around or north of 32.5°S based on satellite imagery. While most of these studies were focused on large (O(100 km)) cyclonic structures south of the EAC separation zone, they all appeared to have been related to smaller frontal eddies advected from further north.

Frontal eddies (also referred to as "spin-up" or "spin-off" eddies) were first identified from sea surface temperature (SST) images, and reversals in near-surface current meter records along the Gulf Stream that were not associated with wind stress nor tides [*Lee*, 1975; *Lee and Mayer*, 1977]. They have characteristic cold cores and form a sharp density front with the filament of warm water from the WBC encircling the structure. Frontal eddies are formed from meanders resulting from mixed barotropic and baroclinic instabilities of the flow, while topographic constraints strongly influence the growth and decay of the structures [*Oey*, 1988; *Gula et al.*, 2015]. They have typical length scales of O(10–50 km) [*Haus et al.*, 2000] and are advected downstream with the meanders of the flow. The advection velocities of frontal eddies in the Gulf Stream (0.2–0.8 m s^{-1}) [*Lee and Atkinson*, 1983; *Archer et al.*, 2015] are typically faster than in the Kuroshio (0.15–0.3 m s^{-1}) [*Itoh and Sugimoto*, 2008 and references therein], due to a shallower shelf and faster transport [*James et al.*, 1999].

Identification of eddy structures has been facilitated with the development of high-frequency (HF) radar technology, that allows high-resolution measurements of surface velocity fields with continuous spatial and temporal coverage [*Paduan and Washburn*, 2013]. In particular, HF or very high-frequency (VHF) radars have been shown to be a powerful tool with which to characterize submesoscale to mesoscale structures over long time periods. For instance, *Kim* [2010] presented the statistics of submesoscale eddies off San Diego, based on around 700 structures detected over a 2 year period. *Kirincich* [2016] was able to analyze the drivers of 2–5 km diameter eddies off Massachusetts that lasted only a few hours but had a great impact on cross-shelf water exchanges. HF radar observations, in combination with modeling experiments, also

revealed the driving mechanisms of a recurring anticyclonic mesoscale eddy off Marseilles in the Mediterranean sea [*Schaeffer et al.*, 2011]. In a WBC similar to the EAC, *Shay et al.* [1998] observed submesoscale vortices along the Florida current that were trapped in the near-inertial band. The authors concluded that these structures were more-likely related to local wind-driven processes and trapped near-inertial waves than associated with spin-off eddies forced by frontal instabilities of the Florida current. In the same region however, *Limouzy-Paris et al.* [1997], *Haus et al.* [2000], and *Archer et al.* [2015] observed isolated frontal eddies passing through the radar domain. The two cyclonic eddies described by *Haus et al.* [2000] were advected by the Florida current at 0.53 and 0.80 m s^{-1} with horizontal scales between 10 and 47 km. *Archer et al.* [2015] showed a similar structure associated with a meander of the current, characterized by intensified surface divergence and SST anomaly of more than 1°C. The effect of frontal eddies on biology was studied more in detail by *Limouzy-Paris et al.* [1997]. They showed that frontal eddies allow entrainment and recruitment of fish larvae in the adjacent coral reefs, as previously suggested by *Lee et al.* [1992].

In the South Pacific, little is known about frontal eddies along the EAC, their frequency of occurrence, their dynamics, and kinematics. For instance, Figure 1 shows a typical instability of the warm EAC with frontal structures influencing the sea surface temperature and chlorophyll-a concentration at the inshore edge of the WBC. Considering the spatial scales of these structures, too small to be resolved by altimetry, surface current velocity from HF radars provide a useful tool for their identification. This present study uses remote sensing measurements from ocean HF radars, satellite images, and in situ mooring observations, to characterize cyclonic eddies that formed near the coast over a 12 month period, upstream of the EAC separation region (Eastern Australia, 30°S), with a particular emphasis on submesoscale frontal eddies. The manuscript is organized as follow. After describing the data set and methods, we focus on the dynamics of a few specific events, before presenting a census of cyclonic eddies identified and tracked in the region over the whole year. We finally discuss the new findings regarding frontal eddies of the EAC and the expected biological implications.

Submesoscale features have been alternately defined based on horizontal length scales or a dynamical definition using the Rossby and Richardson numbers [*Thomas et al.*, 2008]. Here we use the dynamical definition of submesoscale, as processes characterized by Rossby numbers O(1), hence with a relative vorticity of the order of the Coriolis parameter, but we cannot calculate the Richardson number from our observations. Note that the inshore radius of most of the structures we focus on in this paper is also less than the first baroclinic Rossby radius of deformation, which is ∼12–15 km in the region [*Schaeffer et al.*, 2014a].

2. Materials and Methods

2.1. The Data Set

In 2012, as part of Australia's Integrated Marine Observing system (https://portal.aodn.org.au/), two HF radar systems were deployed off Coffs Harbour NSW at ∼30°S (Figure 1) [*Wyatt*, 2015]. HF radars emit radio waves that are backscattered by sea surface gravity waves before returning toward the receiving antennas. Ocean sea surface currents cause a Doppler shift in the backscatter signal from which we can estimate the current velocity given the frequency and bandwidth of the emitted signal [*Paduan and Washburn*, 2013]. Velocities are estimated from radial current speeds measured at two locations. We use an estimate of surface current velocity vectors from 14 September 2012 to 31 September 2013 (UTC), using two WERA phased-array stations (Red Rock, 30.0°S and North Nambucca, 30.6°S) that are setup to transmit every 10 min at a frequency of 13.92 MHz with a 100 kHz bandwidth, with receiving arrays of 16 antennas. The horizontal resolution of the measurements is of 1.5 km and 10.36° in the radial and azimuthal directions, respectively, and the coverage reaches 150 km (Figure 1).

Quality control was first performed on the radial velocities, removing velocities > 3 m s^{-1} and Bragg signal to noise ratio values <8. Velocity vectors were then gridded into a 1.5 km rectangular grid (u and v components), and averaged into hourly values, keeping only hours with ≥3 good measurements out of the 7 readings over the hour (e.g., 09:30, 09:40, 09:50, 10:00, 10:10, 10:20, 10:30). Based on the geometric dilution of precision, values corresponding to intersection angles ≥140° or ≤40° were disregarded. Current speeds $\sqrt{u^2+v^2}$ ≥3 m s^{-1} and velocity components larger than the mean plus 5 times the standard deviation (calculated from the 1 year data set at each point) were also removed. Grid cells with less than 70% of temporal coverage were disregarded, leading to a reduced but relatively consistent spatial coverage over time. The

original and resulting spatial coverage are shown in Figure 1. The estimated accuracy related to the instrument settings and data processing, including the hourly averaging, is of 1.6 cm s^{-1} (L. Wyatt, personal communication, 2017).

Tidal and inertial fluctuations were filtered out using the PL-64 low-pass filter (half amplitude 33 hour, half power 38 h) [*Rosenfeld*, 1983]. Finally, in order to smooth the velocity field and filter out remaining noise, these hourly detided velocities were spatially averaged over nine cells with a running mean (three cells in the zonal and three cells in the meridional direction, leading to two overlapping cells in each direction). This is especially necessary for the calculation of diagnostics like divergence, that are very sensitive to small-scale noise and spatial variability [*Kaplan and Largier*, 2006]. Resulting values are independent every three cells (4.5 km).

Additionally we use moored temperature and current velocity observations at two locations at 30.27°S, CH070 and CH100, over the 70 and 100 m isobaths, respectively. These measurements have a temporal resolution of 5 min and a vertical resolution of 8 m from the bottom to around 20 m from the surface. More detail on the mooring instrumentation is available in *Schaeffer et al.* [2013, 2014b]. Daily satellite sea surface temperature measurements were obtained from AVHRR (L3S 3 day composite products, resolution of ~2 km) and MODIS AQUA which also provides ocean color products of chlorophyll-a concentration (L3 product, resolution of ~1 km). All data are freely available at https://portal.aodn.org.au/.

Wind time series were extracted from the closest land-based meteorological station (Coffs Harbour, 30.31°S, 153.12°E) maintained by the Australian Bureau of Meteorology (BOM) as no over-ocean wind measurement exists in the area. Wind stress was calculated as in *Schaeffer et al.* [2014a], rotated into cross-shelf and along-shelf components using an angle of 20° based on the coastline orientation. The consistency of this land-based station with regional over-ocean wind fields was confirmed using the 12 km and 6 hourly resolution meteorological model ACCESS (Australian Community Climate and Earth System Simulator) [*Puri et al.*, 2013]. Despite having greater intensity than the observations, modeled winds at the BOM station location are highly correlated with in situ measurements (0.93 and 0.60 for meridional and zonal components, respectively), giving some confidence in the modeled data set. Correlations between modeled wind velocities at the location of the station, and velocities averaged over the whole radar domain were also high (0.96 and 0.87 for meridional and zonal components, respectively), showing the spatial representativeness of the over-land wind reversals.

2.2. Diagnostics

In order to understand the flow kinematics in the region, we calculate various diagnostics. Horizontal divergence (δ), vorticity (ζ), strain (ϱ, the square root of the sum of the square of shearing strain and the square of normal strain), Okubo-Weiss parameter (*OW*), and instantaneous rate of separation (IROS) [*Archer et al.*, 2015] are computed following:

$$\delta = \frac{\partial u}{\partial x} + \frac{\partial v}{\partial y} \tag{1}$$

$$\zeta = \frac{\partial v}{\partial x} - \frac{\partial u}{\partial y} \tag{2}$$

$$\varrho = \sqrt{\left(\frac{\partial v}{\partial x} + \frac{\partial u}{\partial y}\right)^2 + \left(\frac{\partial u}{\partial x} - \frac{\partial v}{\partial y}\right)^2} \tag{3}$$

$$OW = \varrho^2 - \zeta^2 \tag{4}$$

$$IROS = \delta + \varrho \tag{5}$$

The IROS is based on the rate of strain and divergence in the flow field and represents the zero order Lagrangian rate of separation at a time t = 0 [*Futch*, 2009]. From this, one can estimate particle separation from a snapshot without integrating the flow over time. The Rossby number is defined as the vorticity normalized by the absolute Coriolis parameter, $R_o = \zeta/|f|$. Differentiation in the zonal (*x*) and meridional (*y*) directions are computed from the gridded surface current velocity field (*u, v*) and central differences (for instance $\frac{\partial u}{\partial x} = \frac{1}{2dx}(u(x+dx,y) - u(x-dx,y))$ with *dx* the interval in the *x* direction).

2.3. Eddy Detection and Characterization

We use an eddy tracking algorithm based on the geometry of the velocity vectors from *Nencioli et al.* [2010] to identify eddies, instead of visual or automatic detection based on the Okubo-Weiss (OW) parameter, wavelets, or winding angle methods [see *Kim*, 2010 for more techniques of identification]. A geometry-based technique was partly selected because submesoscale eddies do not present a typical OW pattern (vorticity dominating at the core and strain at the edge) [*Mahadevan*, 2016 and discussion below]. Eddies were identified following four constraints on the velocity field. It first requires a sign inversion in the zonal (meridional) components and an increase of magnitude *a* points away from the potential center along the meridional (zonal) transects. The center is then defined as the local minimum in a square of length *b* around the selected point, and the rotation sense of the velocity vectors is checked for each quadrant in a square of the length *a-1* (all details in *Nencioli et al.* [2010]). We use a set of parameters $a = 4$ and $b = 3$, that allows the detection of structures with a minimum radius of 6 km, consistent with the study of *Nencioli et al.* [2010]. Using greater parameters (e.g., $a = 8$ and $b = 7$) led to a reduced number of eddy detections due to the different length scales considered and missing detection for structures close to the edge of the coverage. However, eddies with radius >10 km showed similar characteristics regardless of the parameters. Eddies of the same rotation direction within 20 km of each other over less than 1 day are considered to be part of an eddy time series. We define the persistence of an eddy as the time between its first and last detection within the radar domain, and the mean advection speed is calculated as the persistence over the total distance covered. Eddies with only two individual detections were disregarded. For each hourly detection, different parameters are extracted, including zonal and meridional velocity crossing the center, vorticity, and divergence. The furthest closed streamline around the center of the eddy, calculated following *Nencioli et al.* [2010], is used to fit an ellipse characterized by its eccentricity and rotation angle. Due to the high non linearity and asymmetry of the eddies, the radius of the eddy is separated by quadrant, computed as the distance from the center where the tangential velocity peaks along zonal and meridional sections. Note that due to the strong background EAC flow on the eastern and sometimes southern side of the structures, we consider the inshore (western) radius to be characteristic from the eddy length scales. Finally, environmental conditions are also extracted for each time step, including the wind stress and the EAC speed, defined as the maximum southward velocity at the center's latitude.

3. Kinematics and Dynamic Variability

In this section, we focus on a number of distinctive surface circulation features identified during the 12 month period. Namely, we detail the kinematics and dynamical variability of a large cyclonic (cold core) eddy, an EAC meander and a smaller frontal eddy. We contrast these distinctive features with the mean circulation in the region.

3.1. Mean

The presence of the EAC near the coast is clearly apparent in the mean surface fields, revealing a warm (23–24°C) southward current with speeds reaching 1.1 m s^{-1} at 30.1°S (Figure 2). The core of the current is located above the continental slope (2000–3000 m isobaths), ~45–50 km from the coast, following the bathymetric contours. Along its path, the mean current decreases in speed to 0.9 m s^{-1} at 30.6°S. A sharp cross-shelf temperature front of 4°C is formed between the EAC (mean surface temperature of 23°C) and the coastal waters (temperatures around 19°C) (Figure 2a). The mean flow has a characteristic negative relative vorticity at the inshore edge and positive at the offshore edge of O(0.4f) (Figure 2b) and a larger impact on particle separation (IROS) along the inshore edge of the front (Figure 2c).

3.2. Cyclonic Eddy

The largest cyclonic eddy observed during the period extends over the entire radar domain, with an inshore radius of 21 km (Figure 3). The simultaneous SST picture shows a characteristic cold core where temperature in the eddy center is 3–4°C cooler than that over the shelf and in the adjacent EAC (Figure 3a). This CCE is characterized by tangential velocities of up to 1.3 m s^{-1} and strong negative vorticity up to 3.5f (Figure 3e) that dominates over strain in the eddy center, as evidenced by the negative value of the OW parameter (Figure 3f). However, the eddy is profoundly asymmetric, leading to an enhanced shear in the along-shelf axis matching the elongation of the structure (Figure 3d). Horizontal divergence (Figure 3c) also shows an interesting pattern with patches of positive divergence at the south-west and north-east corner of the
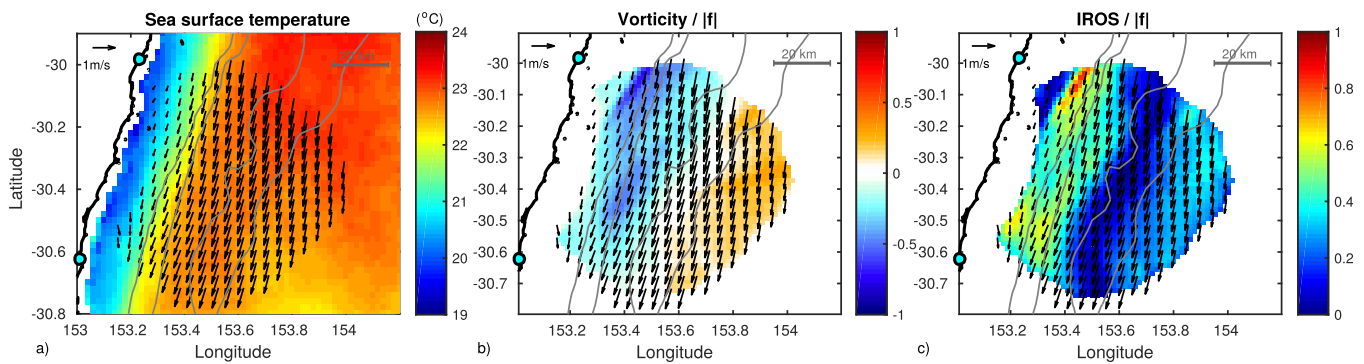
Figure 2. Mean (September 2012–2013) fields of (a) SST ((°C), calculated from monthly AVHRR L3S products), (b) vorticity, and (c) instantaneous rate of separation (IROS). All quantities are detailed in section 2.2. IROS and vorticity are normalized by the absolute value of the Coriolis parameter (leading to Rossby number in panel e). Mean velocity vectors (plots every third point) are overlaid in each plot. The coastline and 100, 200, 2000, and 4000 m isobaths are shown. Blue dots indicate the location of the two HF Radar systems.

structure, rather than at the center, as would be expected from a traditional conceptual model of eddy-pumping. This is in agreement with *Nardelli* [2013] who showed most intense vertical velocities at the periphery of a mesoscale cyclonic eddy. The asymmetry of the CCE also creates a zone of enhanced particle dispersion aligned with the eddy's major axis over the 1000 m topographic contour, as indicated by high values of IROS parameter (Figure 3b).

3.3. Meander and Frontal Eddy

Areas of enhanced particle dispersion can also appear at the inshore edge of the EAC in the absence of a cyclonic eddy, e.g., on 5 December 2012 (Figure 4b). The edge of the intense and narrow current, reaching 2 m s^{-1}, creates a sharp SST gradient of ∼5°C over a few kilometers, also associated with enhanced strain and vorticity of the order 2–4f (Figures 4a, 4d, and 4e). Both the SST and velocity field show the curvature of a meander with a crest and a trough around 30.6°S and 30.3°S, respectively, leading to alternate patches of
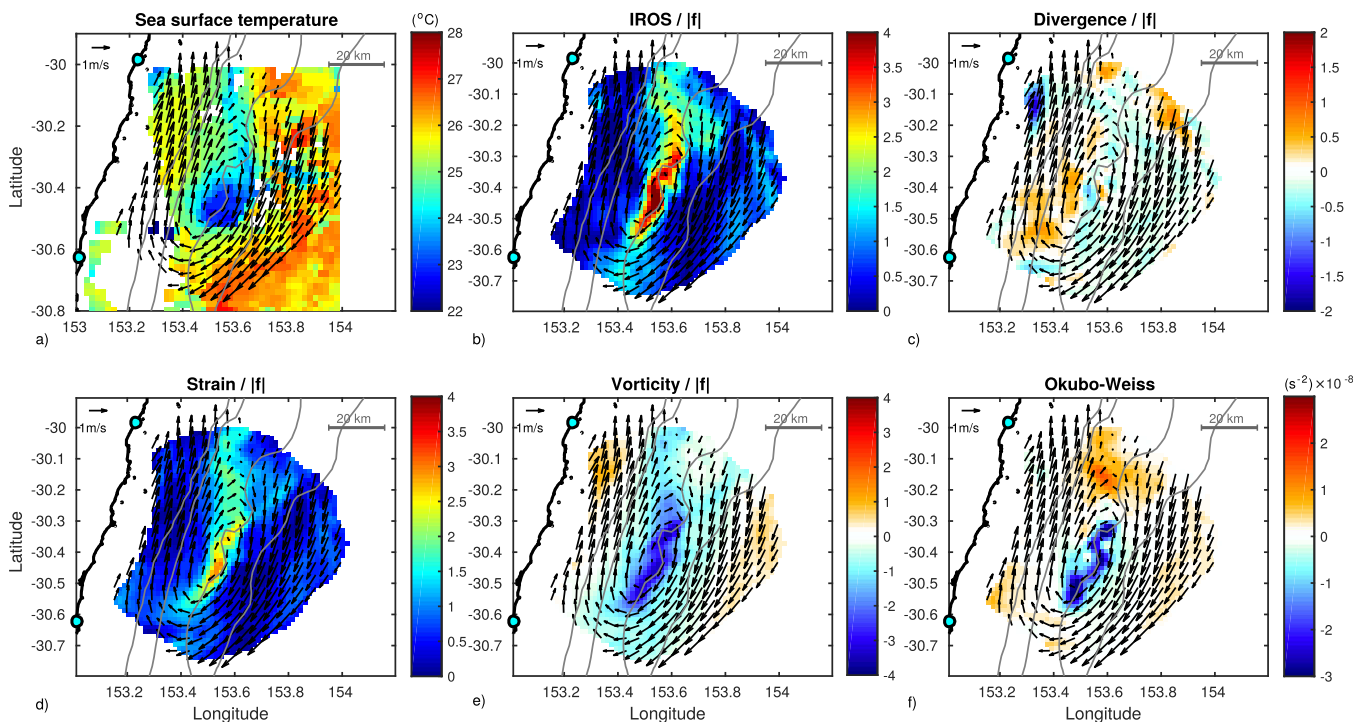

Figure 3. Instantaneous fields on 3 February 2013 17:00h, corresponding to the identification of a cyclonic (cold core) eddy, showing (a) SST (°C, daily AVHRR L3S products), (b) instantaneous rate of separation (IROS), (c) divergence (blue shows zones of convergence), (d) strain, (e) vorticity, and (f) Okubo-Weiss parameter (s^{-2}). All quantities are detailed in section 2.2. IROS, divergence, strain, and vorticity are normalized by the absolute value of the Coriolis parameter (leading to Rossby number in Figure 3e). Instantaneous vectors (plots every third point) are overlaid in each plot. The coastline and 100, 200, 2000, and 4000 m isobaths are shown. Blue dots indicate the location of the two HF Radar systems.
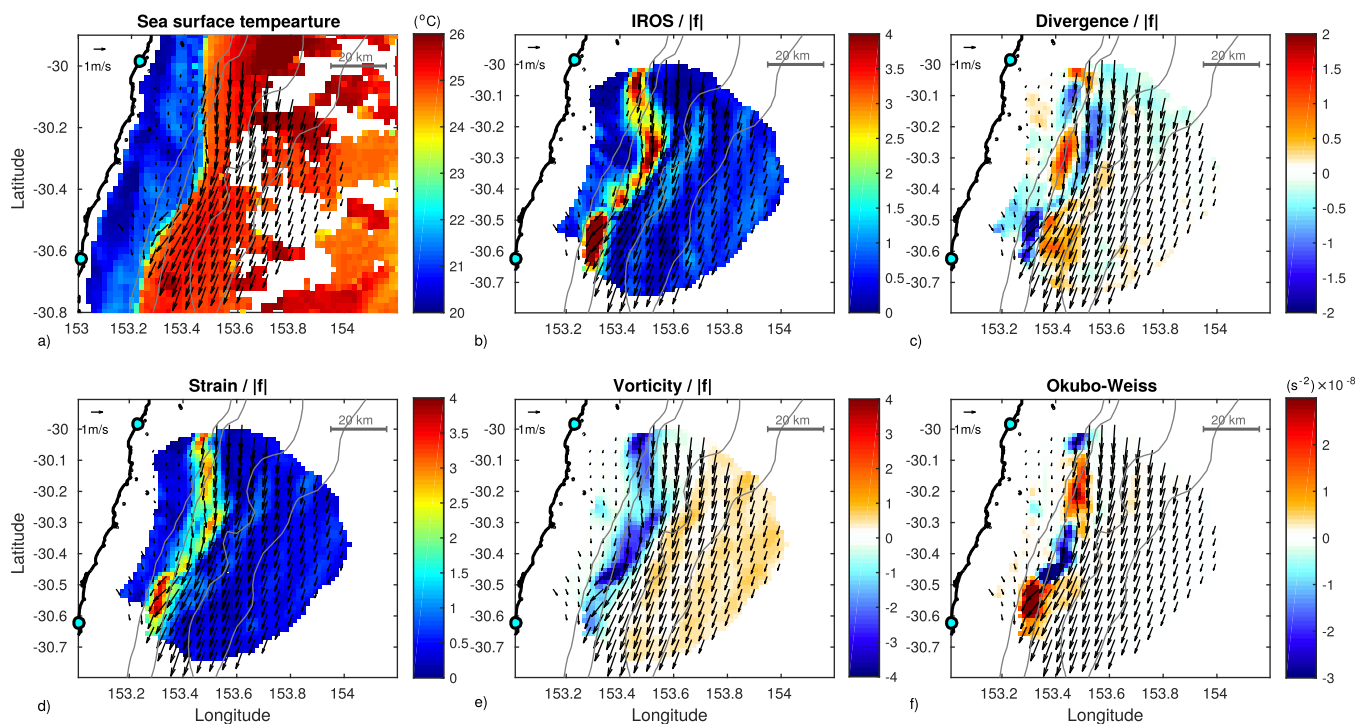
Figure 4. Same as in Figure 3 for an instantaneous snapshot on 5 December 2012 01:00h, corresponding to the identification of an EAC meander.

dominant strain and vorticity along the front (see the OW parameter, Figure 4f). Zones of high convergence and divergence also alternate along the axis of the front (Figure 4c), and in the cross-shelf direction, showing the complexity of submesoscale processes associated with the unstable EAC front.

In some cases, meanders evolve to form a well-defined eddy with closed streamlines, characterized by a cyclonic rotation when on the inshore edge of the current. Figure 5 shows such an event, this time in the middle of winter (29 July 2013). No cloud-free SST image was available on that day; however, SST the following day shows shelf and EAC waters of ~19.5 and 22.5°C, respectively. The Okubo-Weiss parameter shows a similar pattern with enhanced vorticity at the trough, which now corresponds to the location of the cyclonic eddy, and enhanced strain downstream (and to some extent upstream) (Figure 4f). The main difference between the meander in Figure 4 and the frontal eddy in Figure 5 is the pattern associated with divergence. In contrast to patches of a few kilometers, the frontal eddy generates large areas of intensified horizontal divergence at its leading edge (downstream of the eddy) and convergence on its trailing edge (upstream) (Figure 4c), expected to drive upward and downward vertical velocities, respectively (by continuity). This characteristic positive-negative signature was shown for vertical velocities in meanders and frontal eddies in the Gulf Stream as early as *Oey* [1988]; *Bower* [1989] and recently modeled by *Gula et al.* [2016].

4. Eddy Characteristics

4.1. Okubo-Weiss Parameter

Two methods were used to look into the evolution of the eddies and meanders. First we used the OW parameter to highlight episodes of high vorticity dominating the kinematics of the flow. Figures 6a and 6b show the value of the minimum OW parameter (OW < 0, i.e., maximum vorticity compared to strain) obtained across the shelf, for each time step and latitude over two 5 day periods. Lines of high vorticity are evident over a number of periods, e.g., early January 2013 and late July 2013, which are shown in Figure 6. These lines are oblique, and show a signal propagating over latitude and time, corresponding to patches of high vorticity often associated with meanders and frontal eddies as shown in Figures 4 and 5. The corresponding propagation speed was calculated from a Radon transform, used to determine the angle of the strongest signal peak for subsamples. This technique is often used in image processing [e.g., *Almar et al.*, 2016] and has also been successfully applied to estimate eddy propagation [*Chelton et al.*, 2007]. We find a
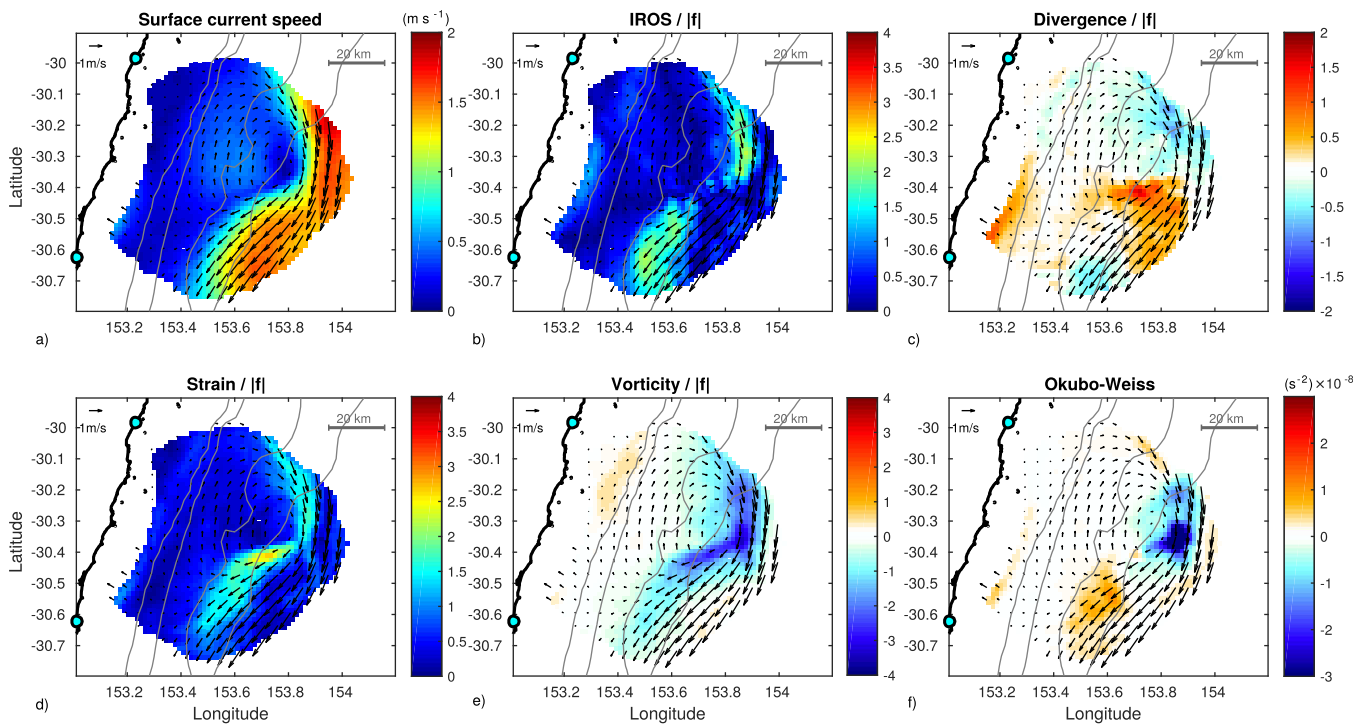
Figure 5. Same as in Figure 3 for an instantaneous snapshot on 29 July 2013 04:00h, corresponding to the identification of a frontal eddy. As SST data were cloud affected, colors in Figure 5a show the current speed.
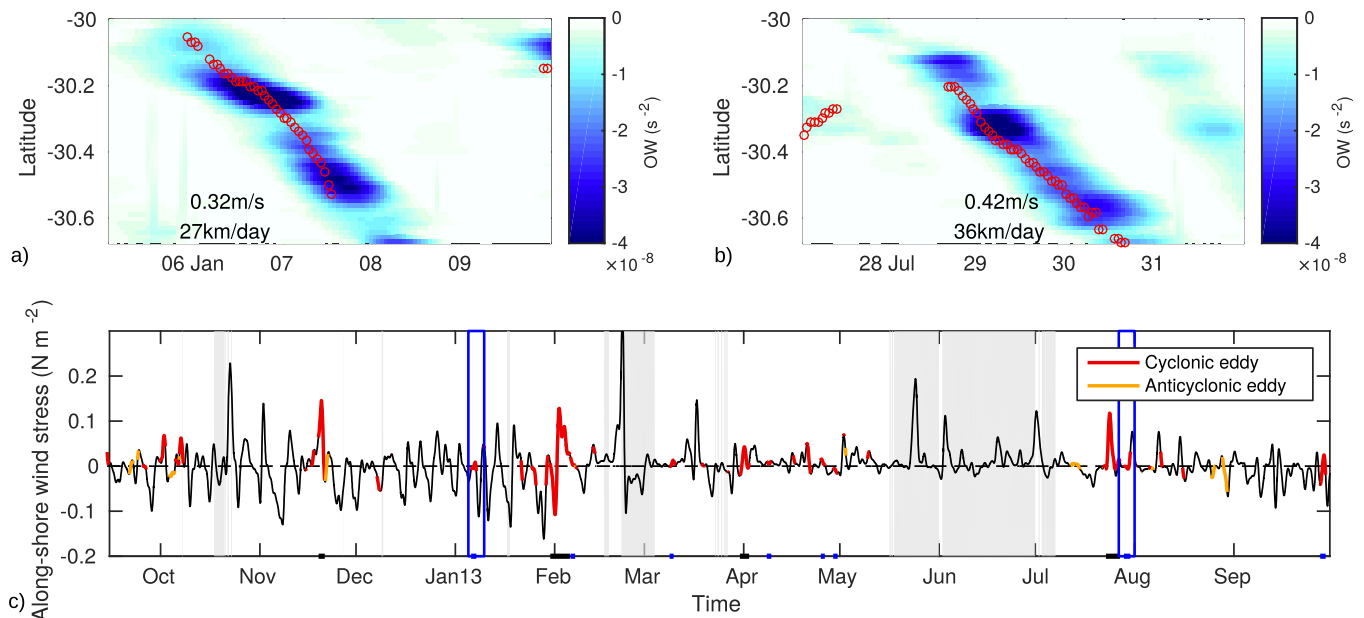

Figure 6. (a and b) Hovmoller plot of the minimum Okubo-Weiss parameter across the shelf (blue colorbar) for two specific events, with the corresponding propagation speed calculated from the Radon transform. Times when cyclonic eddies were detected using the geometric detection algorithm are superimposed, indicated by the red circles. (c) Time series of filtered along-shelf wind stress measurement at Coffs Harbour BOM station (30.31°S, 153.12°E, black line). Oceanographic convention is used (showing direction the wind is blowing to). Times when cyclonic (red) and anticyclonic (orange) eddies were identified are indicated. Gaps in HF radar observations are shown by the light grey shadings. Along the x axis, blue and black thick lines indicate times of eddies categorized as frontal and wind-influenced, respectively. Blue rectangles indicate time periods shown in Figures 6a and 6b.
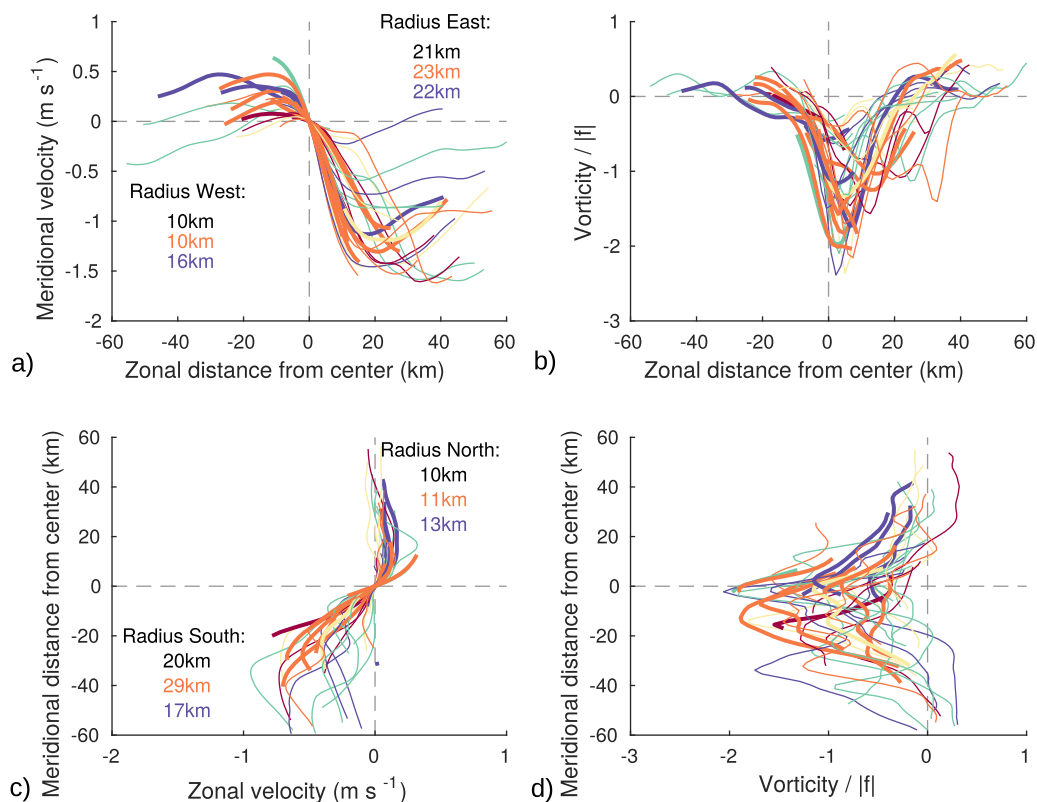
Figure 7. Horizontal structure of cyclonic eddies with persistences >6 h (19 eddies). (a and b) West-East transect of mean meridional velocity and vorticity (normalized by the Coriolis parameter) through the eddy centers. (c and d) South-North transect of mean zonal velocity and vorticity (normalized by the Coriolis parameter) through the eddy centers. Colors refer to the eddy propagation speeds as shown in Figure 8 and bold lines highlight frontal eddies. The mean radii are indicated for each quadrant averaged over all structures (black), frontal eddies (orange), or wind-driven eddies (blue).

southward propagation speed of 0.32–0.42 m s^{-1} (27–36 km d^{-1}) for the six most intense propagation events. Similar results were also obtained when computing the advection speed as the total latitudinal distance traveled by the enhanced vorticity feature over time.

4.2. Eddy Tracking

Eddy structures were also identified using the eddy detection algorithm from *Nencioli et al.* [2010] described in section 2.3, based on different constraints of the velocity field. Times and latitudes of individual hourly eddy detections are overlaid in Figures 6a and 6b (red circles), showing good agreement between patches of high vorticity and well-defined eddy structures (in a geometric sense, as defined in the detection algorithm).

Tracking the individual (hourly) eddy detections over time, we find a total of 40 cyclonic eddies (supporting information Table. SI) and only 16 anticyclonic eddies (probably due to the limited offshore coverage of the data set) over the 12 month period (297 days of good HF radar coverage), hence on average a cyclonic eddy passes through the domain in average every 7 days. There is no seasonality in the occurrence of eddy structures, with detection spanning all seasons (Figure 6c). Persistence of the eddies within the radar domain ranges from hours to 2 days for anticyclones and up to 6 days for cyclones. Note that these values are likely underestimated due to occasional reduced radar coverage. Mean Rossby numbers calculated at the eddy centers (identified from the algorithm) are higher for cyclonic (0.2–1.9, Figure 7 and supporting information Table S1) than for anticyclonic eddies (0.2–0.7). Anticyclonic eddies were in geostrophic balance more than cyclonic eddies, which were often associated with submesoscale dynamics (e.g., with higher Rossby numbers and smaller radii).

The asymmetry of the cyclonic structures is evident when computing the radius in different quadrants (Figures 7a and 7c, supporting information Table S1). The results show an average radius of 10 km for the northern and western side of the cyclones, compared to 20–21 km in the southern and eastern quadrants. In addition, the eccentricity of the streamline ellipses has an average of 0.5, with a mean rotation of −110°
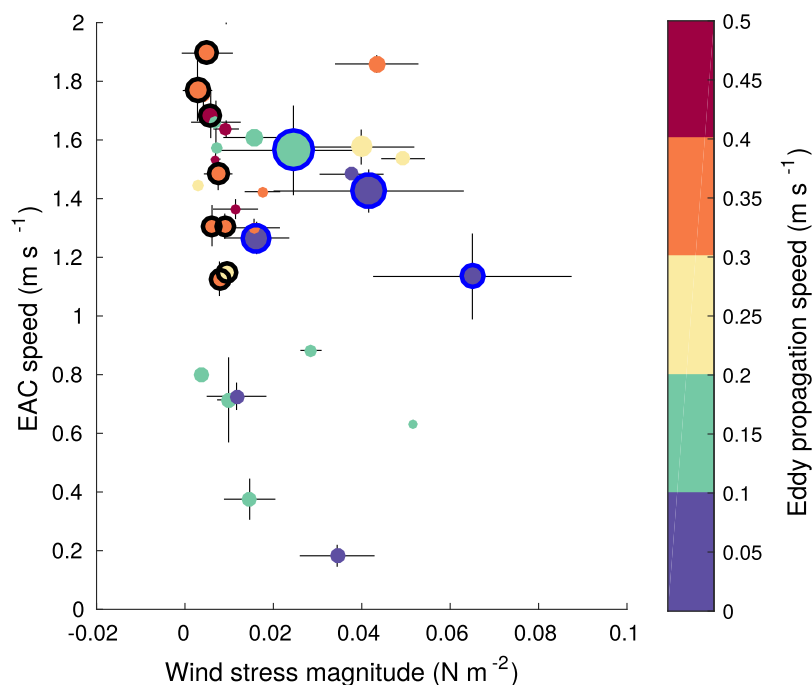
Figure 8. Scatter plot showing all cyclonic eddy detection (with persistences >6 h) as a function of the mean wind stress magnitude and mean EAC speed during the detection. Error bars show the standard deviations corresponding to the eddy life-time. Symbol size is proportional to the eddy persistence (from 6 to 148 h) and colors refer to the eddy propagation speed. Symbols with black contours show the eight events defined as frontal eddies (fast advection speed, strong EAC and weak wind stress) and symbols with blue contours show the four events defined as wind-driven eddies (long persistence, low advection speed, strong wind stress).

from the East, showing the structures are elongated along the shelf. This is in agreement with a much faster flow offshore and downstream for most of the eddies, with a negative vorticity peak also located in the south-eastern quadrant (Figures 7b and 7d).

Cyclonic eddies were identified during a range of conditions, with varying wind stress and EAC strength (supporting information Table S1). Figure 8 summarizes the different cyclonic events, showing no simple relationship. Mean propagation speeds of the structures ranged 0–0.45 m s^{-1}, much less than the range of EAC speeds (0.19–2 m s^{-1}, Figure 8). We were able to distinguish frontal or spin-off eddies, like the ones first characterized by *Lee* [1975], as fast propagating structures during weak wind stress (orange-red dots in Figure 8). They are characterized by southward displacement speeds of 0.25–0.42 m s^{-1}, calculated both using the eddy algorithm and the OW Hovmuller diagram (e.g., Figures 6a and 6b). These structures, like the one described in section 3.3 and illustrated in Figures (5 and 9)a and supporting information Figure S1, are all associated with unstable meanders of the EAC that folded up to form cyclonic eddies. The EAC flow is fast, between 1 and 2 m s^{-1} (Figure 8), and well defined during each of these occurrences (supporting information Figure S1), leading to an enhanced asymmetry with much higher kinetic energy on the EAC (eastern) side of the structures (Figure 9a) and a mean radius much higher in the east and southern quadrants, ∼23–29 km, compared to an inshore radius of 10–11 km (Figure 7, orange lines).

Wind stress seems however to impact the growth and location of some cyclonic eddies. The most persistent structures (supporting information Figure S2) are highlighted in Figure 8 (large blue dots) and remained within the radar domain for between 2 and 6 days. All detections were located near the center of the radar domain, leading to limited advection of the structures (≤0.13 m s^{-1}). While the generation mechanism of these structures is unclear, they all intensified during strong northward wind stress (mean of 0.016–0.06 N m^{-2}). The offshore branches of the eddies are combined with the strong EAC (southward velocities ≥1.2 m s^{-1}), but their inshore sides end up being accentuated (e.g., Figures 3, 9b, and supporting information Figure S2) by a northward flow over the whole shelf in response to the wind stress, leading to larger radius and stronger tangential velocities on the western side than other cyclonic structures (Figure 7). The
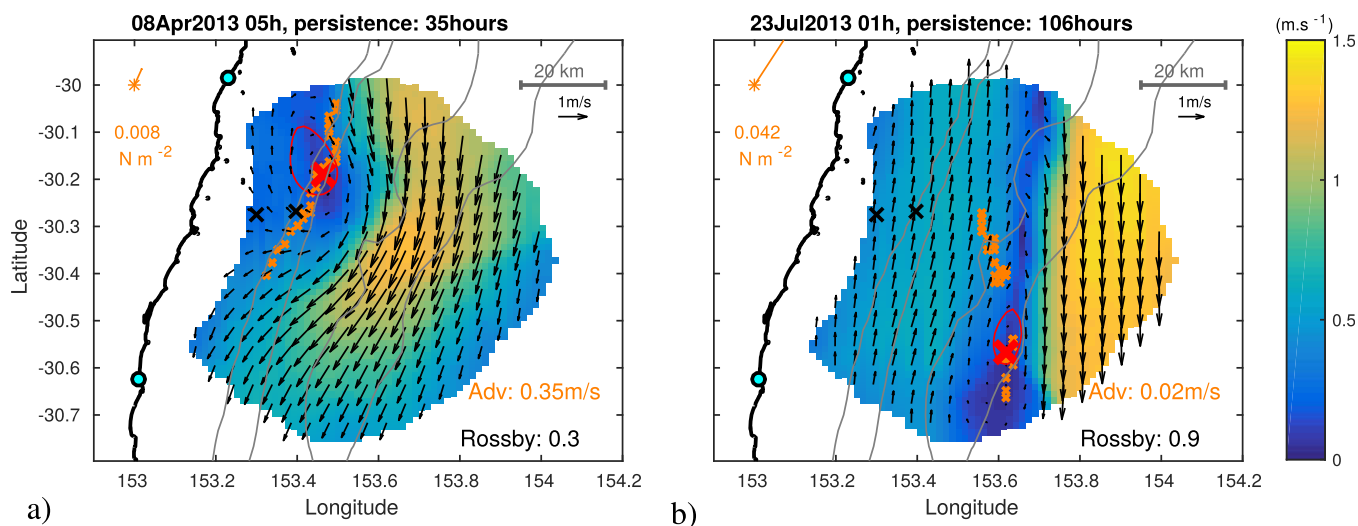
Figure 9. Velocity field and center (red crosses) of (a) a propagating frontal eddy and (b) a wind-driven eddy at mid-life. The date of first detection, duration within the radar coverage (persistence), mean Rossby number, and advection speed are indicated. Orange crosses show the eddy center at different time steps and the red lines indicate the furthest closed streamline around the center at mid-life. Mean wind stress and directions are indicated in top left corners of the subplots (orange). Velocity vectors are plot every third point. The coast-line and 100, 200, 2000, and 4000 m isobaths are shown. Blue dots indicate the location of the two HF Radar systems, and the locations of the two moorings (CH070 inshore and CH100 offshore) are indicated by the black crosses.

streamlines are elongated, with a mean eccentricity of 0.48 compared to an average of 0.5 and 0.57 over all cyclonic structures and the frontal eddies, respectively.

Measurements of wind stress, water temperature, and velocity through the water column are shown in Figure 10 for an eddy detected on the 23 July 2013 (Figure 9b). After a few days characterized by weak wind stress, the onset of an intense northward wind (positive along-shelf wind) is concomitant with the start of a barotropic northward flow (positive along-shelf) at the mooring that lasts as long as the wind is blowing. Due to the location of the mooring relative to the eddy (see Figure 9b), the warm water mass encircling the structure only reaches the mooring after a few hours (Figure 10b). Overall, the strong velocity shear between the offshore southward EAC and the inshore northward wind-driven barotropic current seems to feed the cyclonic eddies (supporting information Figure S2), which grow in diameter and remain locally as long as the wind is blowing. This was also observed with frontal eddies in the Florida Current by *Archer et al.* [2015], who showed that advection was stalled in response to strong opposing winds. Ultimately these eddies grow into large CCEs such as the one described in section 3.2.

5. Discussion

5.1. Frontal Eddies

The propagation of frontal eddies along the inshore edge of the EAC is investigated for the first time using high-resolution continuous current velocities obtained from HF radar. We observed propagation speeds of 0.25–0.4 m s^{-1}, which is slower than in the Gulf Stream (0.2–0.8 m s^{-1}) but faster than in the Kuroshio (0.15–0.3 m s^{-1}). This is not surprising as both the shelf depth and volume transport in our region is mid-range between the deeper shelf along the slower Kuroshio and the shallower shelf along the faster Gulf Stream. As in other WBC regions, the frontal eddies we observed are not generated by local wind stress, but originate from instabilities of the mean flow and propagate poleward through the radar domain. This is con-firmed by Figure 6c, showing different wind conditions during cyclonic eddies, while specific frontal eddies shown in Figures 5, 8, 9a, 11, and supporting information Figure S1, were observed during weak wind stress. *Macdonald et al.* [2016] found that barotropic instabilities were more important than baroclinic and wind-driven processes for the growth of a 100 km diameter cold core eddy downstream of the EAC separation zone. However, the divergence-convergence pattern we find here is characteristic of the theory of baroclinic waves [*Viudez et al.*, 1996]. We therefore suggest that a mix of baroclinic and barotropic instabilities of the EAC drive these meanders, while barotropic processes linked to wind stress or topography influence their growth. In particular, the widening of the shelf and the separation of the EAC could explain the
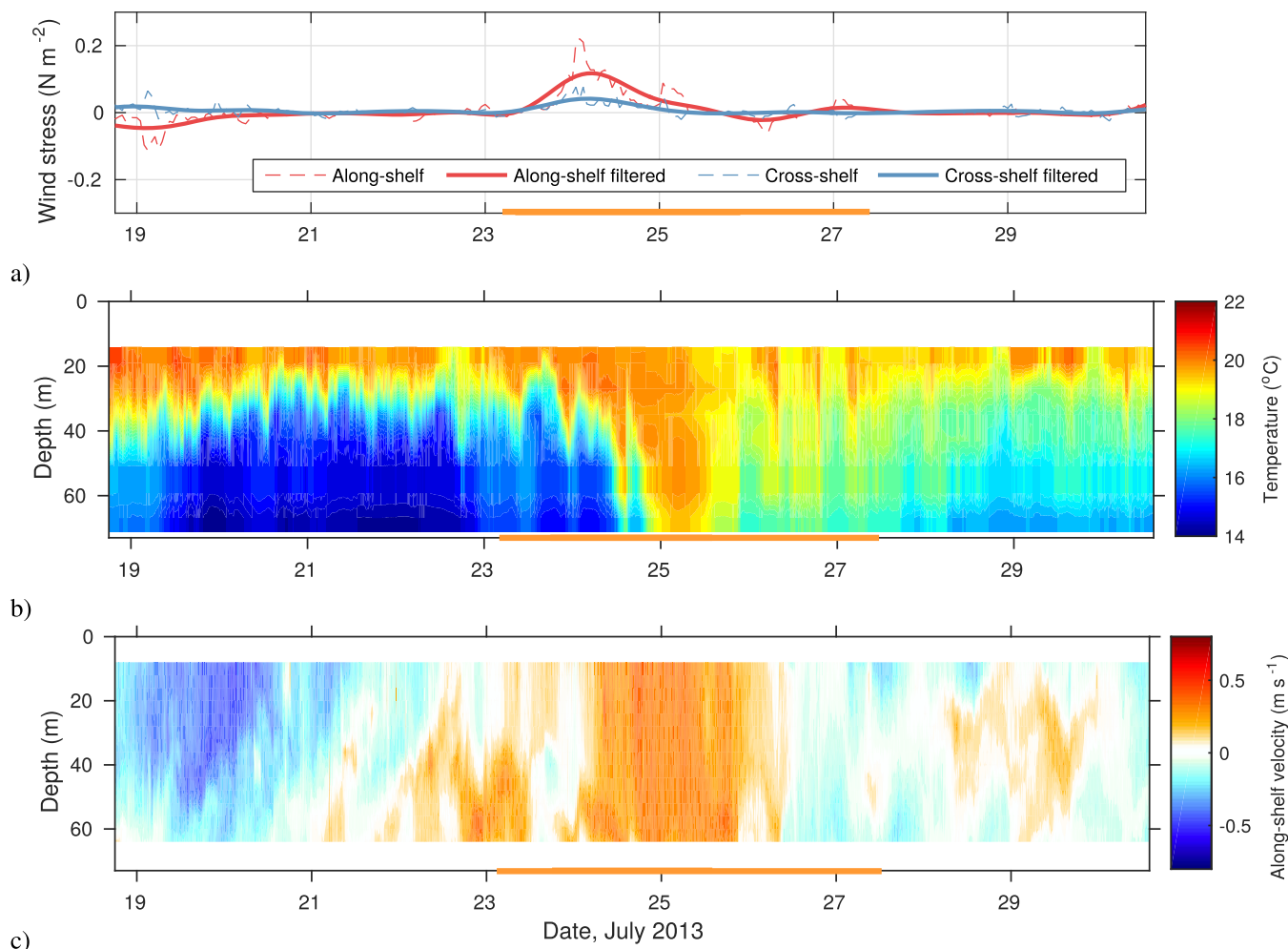
Figure 10. (a) Wind stress, (b) in situ temperature, and) c) along-shelf velocity measured at the 70 m mooring site (CH070) in July 2013. Positive velocities reflect a northward flow. The time of the eddy detection (shown in Figure 9b) is indicated by the orange line. The mooring location is identified in Figure 9b by the black cross.

intensification of frontal eddies into larger and deeper cold core eddies further south, as the ones evidenced by *Macdonald et al.* [2016] and *Mullaney and Suthers* [2013].

5.2. Biological Implications

Frontal eddies have biological implications through both local production and entrainment of biologically rich water. Previous studies showed the characteristic uplift of the isotherms and nutricline in cyclonic eddies, providing nutrients in the euphotic zone for phytoplankton production [*Roughan et al.*, 2017]. In particular, *Everett et al.* [2011] found elevated fluorescence and an abundance of salps (a gelatinous zooplankton) 8 times higher in the center than at the edge of a frontal eddy.

Since HF radars only measure surface currents, vertical dynamics must be inferred from horizontal divergence or complementary in situ observations. Fortunately one of the frontal structures associated with an EAC meander (Figure 9a, detected from 6 April 2013), passed through the in situ mooring array (location of the mooring shown in Figure 9a). The 5 min measurements of temperature and water velocity before, during and after the passage of the structure are shown in Figure 11. The along-shelf currents turn from strong southward to a northward flow during the time the eddy is detected. The cross-shelf component of the current also reverses from negative (onshore) to positive (offshore). Both components suggest an eddy extending over the whole water column (water depth of 100 m). Temperature observations also confirm the uplift of cold water, starting at the first detection of the eddy, when the mooring is sampling the leading edge of the structure. The timing of the uplift matches surface positive divergence calculated from the HF radar
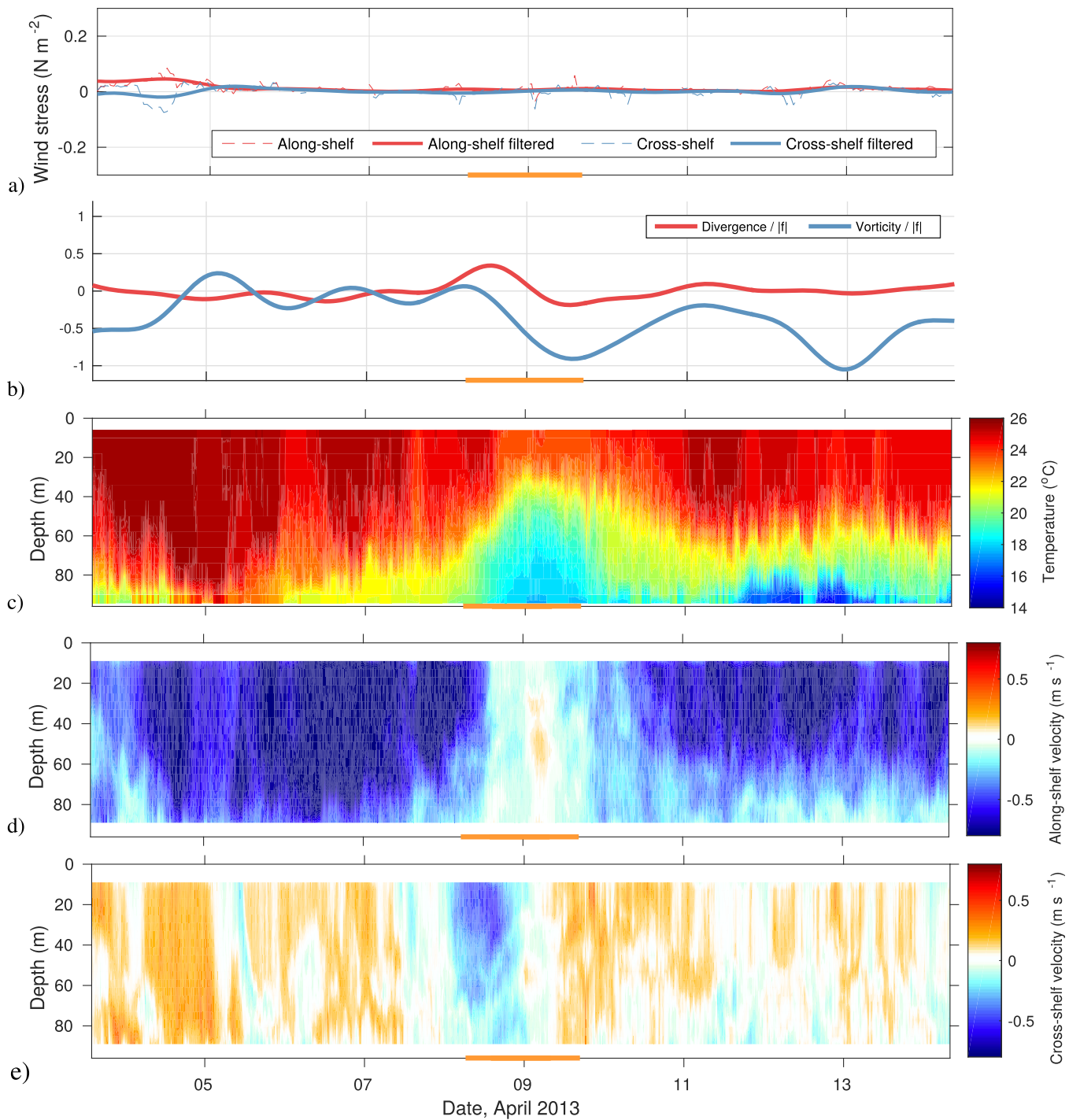
Figure 11. (a) Wind stress, (b) surface vorticity and divergence normalized by the Coriolis parameter, calculated from HF radar currents at the 100 m mooring site, (c) in situ temperature, (d) along-shelf, and (e) cross-shelf velocity measured from the 100 m mooring (CH100) in April 2013. Positive velocities reflect a northward or eastward flow, respectively. The time of the eddy detection (shown in Figure 9a) is indicated by the orange line. The mooring location is identified in Figure 9a by the black cross. The limits of the y axis in Figure 11a were chosen to be similar to Figure 10 to highlight the negligible influence of wind stress for this event.

measurements at the mooring location. The 19°C and 21°C isotherms are uplifted by 35 and 55 m over 10 h and 1 day, respectively. Shallowest measurements at a depth of 8 m show a drop in temperature from 25.2 to 23.8°C over 10 h. *Lee and Atkinson* [1983] found good agreement between the change of position of the isotherms and estimates of vertical velocities. Estimating vertical velocities (*w*) from observations is a difficult task, especially when related to submesoscale dynamics where the geostrophic assumption does not
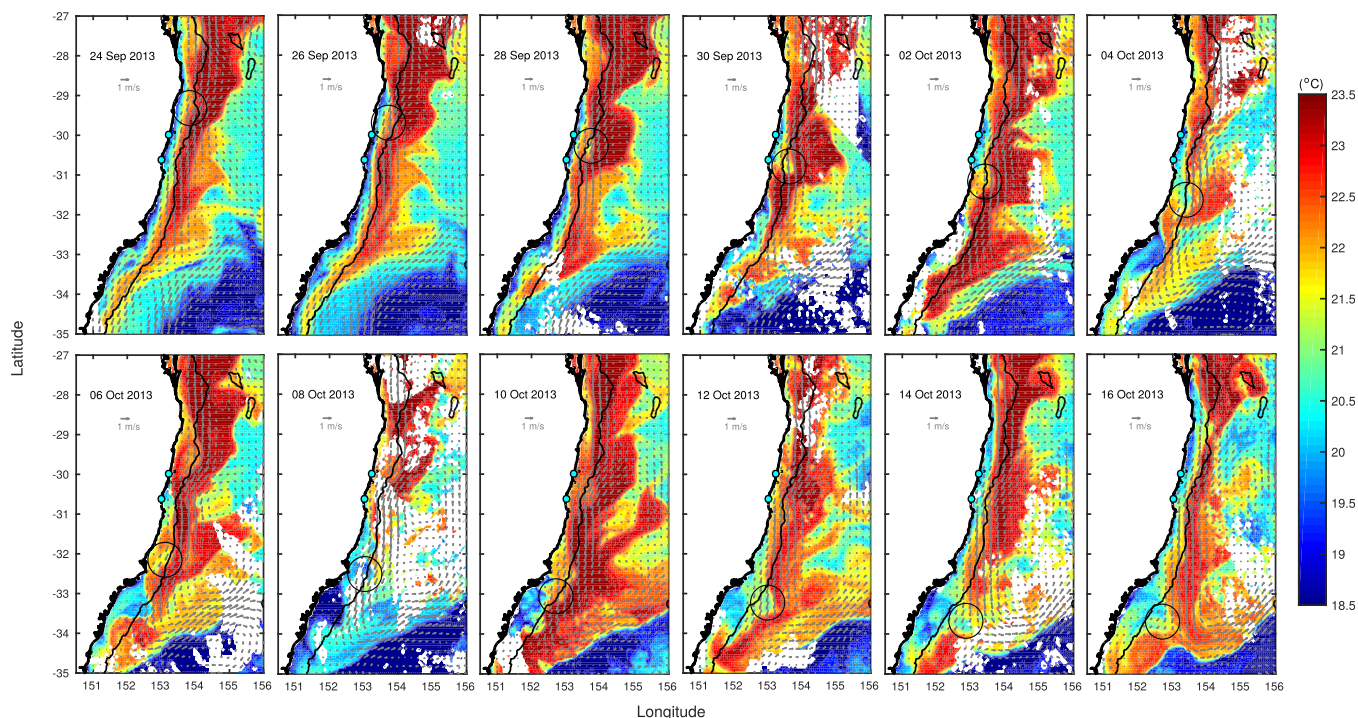
Figure 12. SST (AVHRR L3S) and geostrophic velocity remote sensed images from 24 September 2013 to 16 October 2013 every second day over southeastern Australia, showing the propagation of the frontal eddy presented in Figures 1 and 13. Black circles show the location of the eddy (visual detection of SST) which originates upstream and propagates through the HF radar domain on the 28 September 2013 (panel 3), before separating from the coast ∼ 34°S (last panel). The coastline and 2000 m isobaths are shown. Blue dots indicate the location of the two HF Radar systems.

hold [*Mahadevan*, 2016]. A rough estimate is provided from the equation of continuity leading to $w(h) = h * \delta$ assuming that the horizontal divergence is depth independent in the surface mixed layer (SML) of depth h [*Poulain*, 1993; *Roughan et al.*, 2005]. Typical values of SML were estimated from CH100 temperature measurements and satellite SST time series using a temperature threshold of 0.2 and 0.4°C [see *Schaeffer et al.*, 2014a for similar methods in the bottom mixed layer]. We found 4 years averages (2010–2014) of h = 8 +/- 15 m and h =15 +/- 20 m, respectively, while the SML during early April 2013 (Figure 11c) varies from 30 to 10 m. Therefore, using a SML thickness of 10–30 m and surface divergence of 0.4 |f| (Figure 11b), it results in vertical velocity of 25–75 m d^{-1}, in agreement with the temperature uplift observed. Orders of 10–100 m d^{-1} are typical of submesoscale dynamics, and expected to make a large contribution to phytoplankton production through the uplift of nutrients [*Mahadevan*, 2016]. This is confirmed by the patch of high chlorophyll-a concentration evidenced from satellite imagery in September 2013, which matches the contours of high positive divergence at the leading edge of the frontal eddy (Figure 13).

In addition to local biological production, the proximity of frontal eddies to the coast facilitates the entrainment of productive shelf waters through cross-shelf transport. Using modeled particle tracking, *Everett et al.* [2015] found that >95% of the surface (0–50 m) water mass in a cyclonic eddy originated from the shelf. This was confirmed by glider observations showing the entrainment of cool, high oxygen, and high salinity waters in the eddy. Furthermore *Roughan et al.* [2017] observed high concentrations of coastal larval fish species associated with shelf watermasses in the core of a frontal eddy that had been advected off the shelf. Daily satellite imagery (when not cloudy) enabled us to track the frontal eddies over large distances, well out of the HF radar domain, over time. Figure 12 shows the evolution of the SST over the region, where the frontal eddy from Figures 1 and 13 is shown to have propagated from upstream of the radar domain (at least 29°S) to over 500km to the south (34°S), advected at the inshore edge of the warm EAC. The structure, characterized by a cold core, had an advection speed of 36 km d^{-1} (0.42 m s^{-1}). In addition, it had a strong impact on biology, as shown by Figures 1 and 13. While local production in Figure 13 was probably at the origin of the elevated chlorophyll-a patch when passing the radar coverage, the entrainment of shelf water is clearly visible in Figure 1 for other structures further south (e.g., around 31–33°S), as a tongues of high chlorophyll-a water extending from the coast (upwelling region) around and into an eddy.
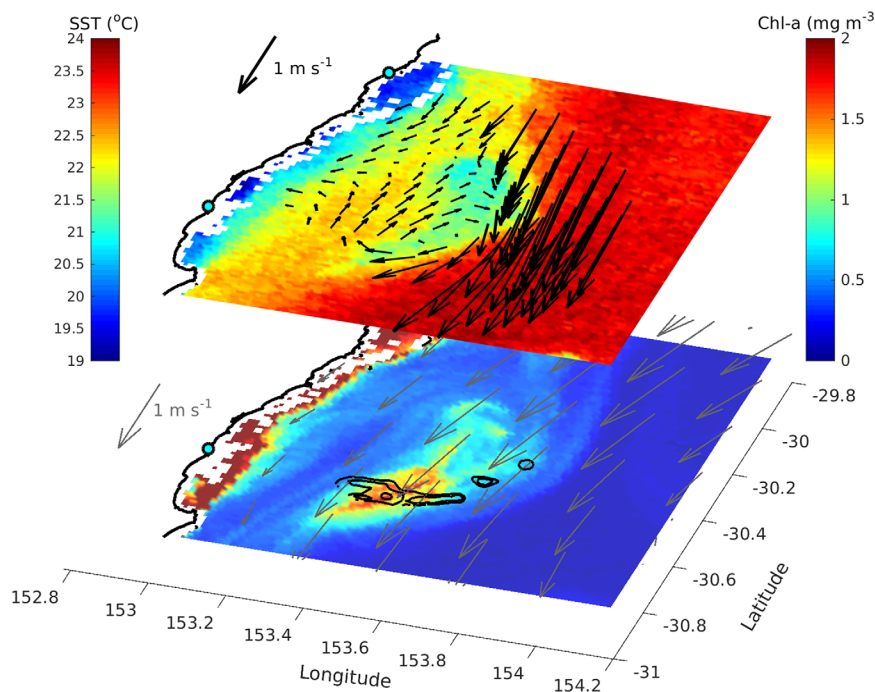
Figure 13. Top view of MODIS SST (top section, left colorbar) and ocean color (bottom, right colorbar) remote-sensed images on 29 September 2013 showing the signature of a frontal eddy. Velocity vectors show the surface currents measured by HF radars on the 29 September 2013 08:00 (plot every sixth grid point, top, black) and geostrophic current from altimetry (bottom, grey). Black contours overlaid on the chlorophyll-a concentrations (bottom) show positive surface divergence calculated from the HF radar velocities (contours of $0.2|f|$, $0.3|f|$, $0.4|f|$, $0.5|f|$, increasing to maximum in the center). Blue dots indicate the location of the two HF Radar systems.

This entrainment can have further implications on the marine food-web, as observed by *Mullaney and Suthers* [2013] when they sampled a cyclonic eddy. They found a greater zooplankton biomass and different fish assemblage than on the adjacent shelf, with a broad range of larval sizes (ages), suggesting that these structures facilitate a successful recruitment though entrainment, enrichment, and retention.

6. Summary

While the first observations of frontal eddies were conducted in the 1970s and 1980s in the Gulf Stream using remote sensing, recent modeling capabilities enabled further understanding of their dynamics [*Gula et al.*, 2016, and references herein]. This is however the first time to our knowledge that the characteristics and kinematics of frontal eddies in a WBC are systematically observed at high resolution. More than 1 year of high-resolution (1.5 km, hourly) surface velocity measurements were obtained using HF radar measurements in the East Australian Current, showing the propagation of frontal eddies and meanders along the eastern coast of Australia. Resolving submesoscale structures in time and space necessitates high-resolution observations, as they are often too small to be captured by altimetry (Figure 13). Our results show that cyclonic eddies from different origins occur all year long and that they form on average every week. They also have a strong ageostrophic circulation with Rossby numbers of up to 1.9 in the core and inshore radii of 10 km on average, hence they are dominated by submesoscale dynamics. Cyclonic eddies that are associated with EAC meanders during weak wind stress propagate downstream with speeds of 0.3–0.4 m s^{-1} (25–35 km d^{-1}). These frontal eddies show the characteristic divergence and convergence patterns at the leading (downstream of the eddy) and trailing edge (upstream), respectively, hence generating upward and downward vertical motion. Cold water anomalies and enhanced chlorophyll-a concentrations from remote sensed data align well with these patches of surface divergence (Figure 13). While EAC meanders and frontal eddies originate from the instabilities in the current upstream and propagate downstream along the WBC, enhanced upfront (southerly) winds drive frontal shear, amplifying their growth, and stalling their propagation. The impact on particle dispersion and biology through local production and entrainment of productive shelf water is expected to be significant in this oligotrophic region.

References

Almar, R., S. Larnier, B. Castelle, T. Scott, and F. Floc'h (2016), On the use of the radon transform to estimate longshore currents from video imagery, *Coastal Eng.*, *114*, 301–308, doi:10.1016/j.coastaleng.2016.04.016.

Archer, M. R., L. K. Shay, B. Jaimes, and J. Martinez-Pedraja (2015), Chapter 11 - observing frontal instabilities of the Florida current using high frequency radar, in *Coastal Ocean Observing Systems*, edited by Y. L. K. H. Weisberg, pp. 179–208, Academic, Boston, Mass., doi: 10.1016/B978-0-12-802022-7.00011-0.

Baird, M. E., and K. R. Ridgway (2012), The southward transport of sub-mesoscale lenses of bass strait water in the centre of anti-cyclonic mesoscale eddies, *Geophys. Res. Letts*, *39*, L02603, doi:10.1029/2011GL050643.

Bower, A. S. (1989), Potential vorticity balances and horizontal divergence along particle trajectories in gulf stream meanders east of cape Hatteras, *J. Phys. Oceanogr.*, *19*(11), 1669–1681.

Cetina-Heredia, P., M. Roughan, E. van Sebille, and M. A. Coleman (2014), Long-term trends in the East Australian Current separation latitude and eddy driven transport, *J. Geophys. Res. Oceans*, *119*, 4351–4366, doi:10.1002/2014JC010071.

Chelton, D. B., M. G. Schlax, R. M. Samelson, and R. A. de Szoeke (2007), Global observations of large oceanic eddies, *Geophys. Res. Lett.*, *34*, L15606, doi:10.1029/2007GL030812.

Everett, J. D., M. E. Baird, and I. M. Suthers (2011), Three-dimensional structure of a swarm of the salp thalia democratica within a cold-core eddy off southeast Australia, *J. Geophys. Res.*, *116*, C12046, doi:10.1029/2011JC007310.

Everett, J. D., M. E. Baird, P. R. Oke, and I. M. Suthers (2012), An avenue of eddies: Quantifying the biophysical properties of mesoscale eddies in the Tasman Sea, *Geophys. Res. Lett.*, *39*, L16608, doi:10.1029/2012GL053091.

Everett, J. D., H. Macdonald, M. E. Baird, J. Humphries, M. Roughan, and I. M. Suthers (2015), Cyclonic entrainment of preconditioned shelf waters into a frontal eddy, *J. Geophys. Res. Oceans*, *120*, 677–691, doi:10.1002/2014JC010301.

Futch, V. (2009), The Lagrangian properties of the flow west of Oahu, Master's thesis, Univ. of Hawaii, Honolulu.

Gula, J., M. J. Molemaker, and J. C. McWilliams (2015), Gulf stream dynamics along the southeastern U.S. seaboard, *J. Phys. Oceanogr.*, *45*(3), 690–715, doi:10.1175/JPO-D-14-0154.1.

Gula, J., M. J. Molemaker, and J. C. McWilliams (2016), Submesoscale dynamics of a Gulf Stream frontal eddy in the south Atlantic bight, *J. Phys. Oceanogr.*, *46*(1), 305–325, doi:10.1175/JPO-D-14-0258.1.

Haus, B., J. Wang, J. Rivera, J. Martinez-Pedraja, and N. Smith (2000), Remote radar measurement of shelf currents off Key Largo, Florida, U.S.A., *Estuarine Coastal Shelf Sci.*, *51*(5), 553–569, doi:10.1006/ecss.2000.0704.

Itoh, S., and T. Sugimoto (2008), Current variability of the Kuroshio near the separation point from the western boundary, *J. Geophys. Res.*, *113*, C11020, doi:10.1029/2007JC004682.

James, C., M. Wimbush, and H. Ichikawa (1999), Kuroshio meanders in the east China sea, *J. Phys. Oceanogr.*, *29*(2), 259–272, doi:10.1175/1520-0485(1999)029<0259:KMITEC>2.0.CO;2.

Kaplan, D. M., and J. Largier (2006), {HF} radar-derived origin and destination of surface waters off Bodega Bay, California, *Deep Sea Res., Part II*, *53*(25–26), 2906–2930, doi:10.1016/j.dsr2.2006.07.012.

Kim, S. Y. (2010), Observations of submesoscale eddies using high-frequency radar-derived kinematic and dynamic quantities, *Cont. Shelf Res.*, *30*(15), 1639–1655, doi:10.1016/j.csr.2010.06.011.

Kirincich, A. (2016), The occurrence, drivers, and implications of submesoscale eddies on the Marthas Vineyard inner shelf, *J. Phys. Oceanogr.*, *46*, 2645–2662. doi:10.1175/JPO-D-15-0191.1.

Lee, T. N. (1975), Florida current spin-off eddies, *Deep Sea Res. Oceanogr. Abstr.*, *22*(11), 753–765, doi:10.1016/0011-7471(75)90080-7.

Lee, T. N., and L. P. Atkinson (1983), Low-frequency current and temperature variability from gulf stream frontal eddies and atmospheric forcing along the southeast U.S. outer continental shelf, *J. Geophys. Res.*, *88*(C8), 4541–4567, doi:10.1029/JC088iC08p04541.

Lee, T. N., and D. Mayer (1977), Low-frequency current variability and spin-off eddies along the shelf off southeast Florida, *J. Mar. Res.*, *35*, 193–220.

Lee, T. N., C. Rooth, E. Williams, M. McGowan, A. F. Szmant, and M. Clarke (1992), Influence of Florida current, gyres and wind-driven circulation on transport of larvae and recruitment in the Florida Keys coral reefs, *Cont. Shelf Res.*, *12*(7), 971–1002, doi:10.1016/0278-4343(92)90055-O.

Limouzy-Paris, C. B., H. C. Graber, D. L. Jones, A. W. Rpke, and W. J. Richards (1997), Translocation of larval coral reef fishes via submesoscale spin-off eddies from the Florida current, *Bull. Mar. Sci.*, *60*(3), 966–983.

Macdonald, H. S., M. Roughan, M. Baird, and J. Wilkin (2016), The formation of a cold-core eddy in the East Australian Current, *Cont. Shelf Res.*, *114*, 72–84, doi:10.1016/j.csr.2016.01.002.

Mahadevan, A. (2016), The impact of submesoscale physics on primary productivity of plankton, *Annu. Rev. Mar. Sci.*, *8*(1), 161–184, doi:10.1146/annurev-marine-010814-015912.

Meinen, C. S., M. O. Baringer, and R. F. Garcia (2010), Florida current transport variability: An analysis of annual and longer-period signals, *Deep Sea Res. Part I*, *57*(7), 835–846, doi:10.1016/j.dsr.2010.04.001.

Mullaney, T. J., and I. M. Suthers (2013), Entrainment and retention of the coastal larval fish assemblage by a short-lived, submesoscale, frontal eddy of the East Australian Current, *Limnol. Oceanogr.*, *58*(5), 1546–1556, doi:10.4319/lo.2013.58.5.1546.

Nardelli, B. B. (2013), Vortex waves and vertical motion in a mesoscale cyclonic eddy, *J. Geophys. Res. Oceans*, *118*, 5609–5624, doi:10.1002/jgrc.20345.

Nencioli, F., C. Dong, T. Dickey, L. Washburn, and J. C. McWilliams (2010), A vector geometry-based eddy detection algorithm and its application to a high-resolution numerical model product and high-frequency radar surface velocities in the southern California bight, *J. Atmos. Oceanic Technol.*, *27*, 564, doi:10.1175/2009JTECHO725.1.

Nilsson, C., and G. Cresswell (1980), The formation and evolution of East Australian Current warm-core eddies, *Prog. Oceanogr.*, *9*(3), 133–183, doi:10.1016/0079-6611(80)90008-7.

Oey, L.-Y. (1988), A model of Gulf Stream frontal instabilities, meanders and eddies along the continental slope, *J. Phys. Oceanogr.*, *18*(2), 211–229, doi:10.1175/1520-0485(1988)018<0211:AMOGSF>2.0.CO;2.

Oke, P. R., and D. A. Griffin (2011), The cold-core eddy and strong upwelling off the coast of New South Wales in early 2007, *Deep Sea Res., Part II*, *58*(5), 574–591, doi:10.1016/j.dsr2.2010.06.006.

Oliver, E. C. J., T. J. O'Kane, and N. J. Holbrook (2015), Projected changes to Tasman sea eddies in a future climate, *J. Geophys. Res. Oceans*, *120*, 7150–7165, doi:10.1002/2015JC010993.

Paduan, J. D., and L. Washburn (2013), High-frequency radar observations of ocean surface currents, *Annu. Rev. Mar. Sci.*, *5*(1), 115–136, doi:10.1146/annurev-marine-121211-172315.

Poulain, P.-M. (1993), Estimates of horizontal divergence and vertical velocity in the equatorial pacific, *J. Phys. Oceanogr.*, *23*(4), 601–607, doi:10.1175/1520-0485(1993)023\<0601:EOHDAV>2.0.CO;2.

Puri, K., et al. (2013), Implementation of the initial access numerical weather prediction system, *Aust. Meteorol. Oceanogr. J*, *63*, 265–284.

Ridgway, K. R. (2007), Long-term trend and decadal variability of the southward penetration of the East Australian Current, *Geophys. Res. Lett.*, *34*, L13613, doi:10.1029/2007GL030393.

Ridgway, K. R., R. C. Coleman, R. J. Bailey, and P. Sutton (2008), Decadal variability of East Australian Current transport inferred from repeated high-density XBT transects, a CTD survey and satellite altimetry, *J. Geophys. Res.*, *113*, C08039, doi:10.1029/2007JC004664.

Rosenfeld, L. (1983), CODE-1: Moored array and large-scale data report, *Tech. Rep. 83-23*, Woods Hole Oceanogr. Inst., Woods Hole, Mass.

Roughan, M., E. J. Terrill, J. L. Largier, and M. P. Otero (2005), Observations of divergence and upwelling around point Loma, California, *J. Geophys. Res.*, *110*, C04011, doi:10.1029/2004JC002662.

Roughan, M., S. R. Keating, A. Schaeffer, P. Cetina Heredia, C. Rocha, D. Griffin, R. Robertson, and I. M. Suthers (2017), A tale of two eddies: The biophysical characteristics of two contrasting cyclonic eddies in the East Australian Current System, *J. Geophys. Res. Oceans*, *122*, 2494–2518, doi:10.1002/2016JC012241.

Schaeffer, A., and M. Roughan (2015), Influence of a western boundary current on shelf dynamics and upwelling from repeat glider deployments, *Geophys. Res. Lett.*, *42*, 121–128, doi:10.1002/2014GL062260.

Schaeffer, A., A. Molcard, P. Forget, P. Frauni, and P. Garreau (2011), Generation mechanisms for mesoscale eddies in the Gulf of Lions: Radar observation and modeling, *Ocean Dyn.*, *61*, 1587–1609.

Schaeffer, A., M. Roughan, and B. Morris (2013), Cross-shelf dynamics in a western boundary current. Implications for upwelling, *J. Phys. Oceanogr.*, *43*, 1042–1059, doi:10.1175/JPO-D-12-0177.1.

Schaeffer, A., M. Roughan, and J. E. Wood (2014a), Observed bottom boundary layer transport and uplift on the continental shelf adjacent to a western boundary current, *J. Geophys. Res. Oceans*, *119*, 4922–4939, doi:10.1002/2013JC009735.

Schaeffer, A., M. Roughan, and B. Morris (2014b), Corrigendum cross-shelf dynamics in a western boundary current. Implications for upwelling, *J. Phys. Oceanogr.*, *44*, 2812–2813, doi:10.1175/JPO-D-14-0091.1.

Shay, L., T. Lee, E. Williams, H. Graber, and C. Rooth (1998), Effects of low frequency current variability on submesoscale near-inertial vortices, *J. Geophys. Res.*, *103*(C9), 18,691–18,714.

Sloyan, B. M., K. R. Ridgway, and R. Cowley (2016), The East Australian Current and property transport at 27°s from 2012 to 2013, *J. Phys. Oceanogr.*, *46*(3), 993–1008, doi:10.1175/JPO-D-15-0052.1.

Thomas, L. N., A. Tandon, and A. Mahadevan (2008), *Submesoscale Processes and Dynamics*, pp. 17–38, AGU, Washington, D. C., doi:10.1029/177GM04.

Viudez, A., J. Tintore, and R. L. Haney (1996), Circulation in the Alboran sea as determined by quasi-synoptic hydrographic observations. Part I: Three-dimensional structure of the two anticyclonic gyres, *J. Phys. Oceanogr.*, *26*(5), 684–705, doi:10.1175/1520-0485(1996)026 < 0684: CITASA>2.0.CO;2.

Wilkin, J., and W. Zhang (2007), Modes of mesoscale sea surface height and temperature variability in the East Australian current, *J. Geophys. Res.*, *112*, C01013, doi:10.1029/2006JC003590.

Wyatt, L. R. (2015), Chapter 9 - the IMOS ocean radar facility, ACORN, in *Coastal Ocean Observing Systems*, edited by Y. L. K. H. Weisberg, pp. 143–158, Academic, Boston, Mass., doi:10.1016/B978-0-12-802022-7.00009-2.